UC Santa Barbara
UC Santa Barbara Previously Published Works

Title

Fast Charging from Low Li-Ion Migration Barriers in WadsleyâRoth NaNb

7

O

18

Anodes

Permalink

Journal

ISSN

Authors

Zohar, Arava
Li, Tianyu
Zhou, Yucheng
et al.

Publication Date

DOI

Peer reviewed

Fast Charging from Low Li–ion Migration Barriers in Wadsley-Roth NaNb$_7$O$_{18}$ Anodes

Arava Zohar,[†] Tianyu Li,[†] Yucheng Zhou,[‡] Kira E. Wyckoff,[†]

Alexander Justice Bologna,[¶] Ashlea Patterson,[†] Laurent Pilon,[‡] and

Ram Seshadri[*,†]

†Materials Department and Materials Research Laboratory

University of California, Santa Barbara, California 93106, United States

‡Mechanical and Aerospace Engineering Department

Henry Samueli School of Engineering and Applied Science

University of California, Los Angeles, California 90095, United States

¶Department of Chemistry and Biochemistry

University of California, Santa Barbara, California 93106, United States

E-mail: seshadri@mrl.ucsb.edu

Abstract

While current electric vehicles are approaching internal combustion engine vehicles in terms of driving range, the relatively long charging time of batteries represents a fundamental challenge. Materials used as anodes show slow ion insertion, which is usually responsible for the inability of automotive batteries to charge rapidly. To address this challenge, research into the kinetics of solid-state ion insertion is needed. The essential properties of fast-charging electrodes include high electronic and ionic conductivity, mechanical and chemical stability, and a 3D framework with channels for ion transport, especially when the added cost of nanostructuring is not desirable. In recent years, there has been increasing recognition that Nb-based shear-structured oxides, many belonging to the Wadsley-Roth class compounds, show fast insertion. We focus here on $NaNb_7O_{18}$, a member of this Wadsley-Roth family that has not been previously studied as an anode material for Li–ion batteries. Bulk $NaNb_7O_{18}$ is shown to demonstrate high cyclability, retaining over 90% capacity even after 1000 cycles at a relatively rapid 2C rate. Potentiometric entropy measurements support the presence of two-phase reaction mechanisms (which is usually contraindicated for fast charging) and point to the role of intralayer ion ordering. The energy barrier between Li sites is found to be low, which is likely to be an important contributor to the fast lithiation kinetics in this compound. A deeper electrochemical analysis points to apparent diffusion coefficients in the range of $10^{-12}\,\mathrm{cm^2\,s^{-1}}$ and low overpotential close to $130\,\mathrm{mV}$. An analysis of the lithiation kinetics of related Wadsley-Roth compounds finds that fast intercalation/deintercalation is robust across this family of compounds regardless of the details of the intercalation mechanism.

2

Introduction

Excess CO_2 emissions are one of the primary causes of climate change, and it is widely agreed that electrification of transportation can help reduce these emissions, wherein rechargeable batteries and electric motors in fuel and power vehicles, rather than hydrocarbon fuels and combustion engines. While rechargeable Li–ion batteries in automobiles have improved their capacities sufficiently so that range is no longer a pressing issue, relatively slow battery charging rates are still an issue. The US Department of Energy has stated the aim of improving battery performance in electric vehicles to achieve a charging experience similar to refueling, which typically takes a few minutes. A battery with fast-charging capability requires a negative electrode (anode) that can intercalate ions rapidly. Over the years, many efforts have focused on increasing the capacity of cathode materials in Li–ion batteries.[1–3] However, the anode material, graphite, has remained largely unchanged. Graphite is widely used as an anode due to its high theoretical Li–ion storage capacity of $372\,\mathrm{mAh\,g^{-1}}$,[4] reversible insertion and abundance. However, its main drawback is a relatively slow charging rate, and increasing the charging rate of graphite electrodes beyond certain low thresholds can cause safety issues. The low voltage for Li–ion insertion in graphite also results in electrolyte decomposition and the formation of a solid electrolyte interphase (SEI), slowing kinetics and reducing efficiency.[5–7] New materials capable of fast charging rates are necessary to bridge the gap between current battery performance and future goals.

New electrode materials for efficient and fast electrochemical energy storage should feature several properties, including high electronic and ionic conductivity, mechanical and chemical stability, suitable redox voltage, and channels in the structure that enable ion insertion. The selected elemental electrode materials should also ideally be non-toxic, accessible, abundant, and possess high specific capacity. Oxides of transition metals such as Ti, V, Nb, and Mo can meet these requirements. These oxides display various crystal structures (*e.g.* rutile, spinel, layered, . . .) which opens exciting opportunities for

discovering materials with high ion diffusivity in electrodes. These elements have redox potentials between 1.0 V and 2.0 V *vs.* Li$^+$/Li, alleviating concerns about safety and stability in this voltage range, as SEI formation and Li dendrite growth are associated with potentials below 1.0 V.

Niobium oxide compounds with crystallographic shear structures, including the Wadsley-Roth compounds, have demonstrated impressive capacity performance and retention at high rates.[8–11] Their capacity can be explained by the multiple stable oxidation states of niobium, allowing for storage of more than one electron *per* transition metal. These multiple oxidation states originate from partially filled d-orbitals, leading to distinctive characteristics such as insulator-to-metal transitions[12] and second-order Jahn-Teller distortions.[13] Both phenomena result from electron occupation that modifies the structure. During cell cycling, these changes can affect charging rate performance. For example, the second-order Jahn-Teller distortion leads to displacement of the metal in the center of the octahedral, potentially creating more space for Li–ions and elevating the diffusion coefficient compared to non-distorted octahedra.[14] This understanding can explain why TiO$_2$ cannot be fully lithiated using electrochemical methods.[15] In addition to acceptable capacity performance, the charging rates of shear-structured niobium oxide structures have been impressive, exceeding 100 mAh g^{-1} within 6 minutes of charging.[12,16–18] These compounds possess corner-shared polyhedra that form open channels for Li–ions, and edge-shared polyhedra that keep the structure stable during cycling.

Ion insertion is usually expected to evolve through two main mechanisms: two-phase reactions or solid solution reactions. A two-phase reaction involves the coexistence of the starting compound with a new phase. This reaction should have a well-defined borderline between the two phases. In a solid-solution reaction, the mobile ion mixes in the existing phase until a new phase forms. A first-principles thermodynamics study has found that a high degree of Li ordering between different sites in the host crystal is associated with two-phase reactions and slow kinetics.[19,20] Conversely, a low degree of Li ordering between

4

different sites in the host crystal lowers the diffusion barrier and is often associated with solid-solution behavior and faster kinetics. Low entropy of Li insertion creates a barrier for more Li–ions to intercalate into subsequent sites.[21] Therefore, an approach to achieve faster kinetics is to reduce Li-ordering by allowing more solid-solution reactions. This approach aligns with that of Clément and Ceder,[22] and shows improved performance and rates when mixing multiple cations in disordered rock-salt cathodes. Cation disorder can thus reduce the degree of Li ordering and allow faster kinetics. For clarity, the term "order" is mentioned from two different perspectives: the ordering of the intercalated Li–ion in the host crystal, as opposed to the ordering of cations in the host, notably in crystals where different metal cations occupy the same crystallographic sites.

In this study, we present a member of the Wadsley-Roth family, $NaNb_7O_{18}$, investigated for the first time as an anode for Li–ion batteries. This composition was introduced in 1984 by Marinder and Sundberg, where was the structure resolved by using high-resolution electron microscopy and multi-slice calculations of simulated images.[23] There are two possible types of sites for Li–ion insertion. Thanks to the high degree of cation order in this compound and the limited number of insertion sites, it can be used as a case study to examine whether the nature of the insertion affects kinetics. We find that $NaNb_7O_{18}$ is an electrode material with impressive capacities at high rates despite displaying two-phase behavior.

To obtain a broader understanding of the manner in which the Wadsley-Roth family hosts Li insertion, we have examined five different compounds using the galvanostatic intermittent titration technique (GITT),[24,25] and extracted diffusion coefficients and overpotentials. The results show a relatively tight range of diffusion coefficients and overpotentials across the different compounds with no particular dependence on the precise nature of Li insertion, whether solid-solution or two-phase reactions.

Materials and Methods

Preparation of NaNb$_7$O$_{18}$

NaNb$_7$O$_{18}$ powders were prepared from stoichiometric amounts of NaNbO$_3$ (Aldrich Chemical Company, 99%) and Nb$_2$O$_5$ (Materion, 99.95%). The starting materials were ground in an agate mortar for 10 min, pressed into 350 mg pellets under 4.0 tons in a 10 mm diameter die, and placed into a 10 cm^3 alumina crucible, which was heated at 800 °C for 24 hr and then at 1150 °C for 48 hr. The sample was slowly cooled to room temperature in the furnace. The preparation of other samples employed in this study are described in the Supporting Information.

Powder Diffraction and Rietveld Refinements

Powder X-ray diffraction (PXRD) measurements were performed using a Panalytical Empyrean powder diffractometer in reflection mode with a Cu Kα radiation source. Rietveld analysis was performed to confirm the structure and phase purity using the TOPAS[26] software package. Crystal structures were visualized using VESTA.[27] High-resolution synchrotron X-ray powder diffraction (SXPD) data were collected at the beamline 2-1 at the Stanford Synchrotron Radiation Source using a wavelength of $\lambda = 0.1173$ Å. A 2D Perkin-Elmer a-Si flat panel detector was used to collect the data.

Operando X-ray diffraction under electrochemical cycling

Operando X-ray diffraction data were collected during electrochemical cycling using an in-house cell with a Be-window. The cell was placed in a Pananalytical Empyrean powder diffractometer in reflection mode with a Cu-Kα radiation source.

Raman Spectroscopy

Raman spectroscopy was performed at room temperature using a Horiba Jobin Yvon T64000 open-frame confocal microscope operating with an excitation laser wavelength of $\lambda = 488$ nm with a monochromator and an LN_2-cooled CCD array detector. Filters were used to reduce the laser to 50% of its original intensity to prevent beam damage to the samples. Spectra were calibrated by referencing the spectrum of monocrystalline silicon, which has a peak at $521 \, cm^{-1}$.

Scanning Electron Microscopy (SEM)

SEM images of powder samples placed on double-sided carbon tape were acquired on a Apreo C FEG (ThermoFisher) microscope using secondary electrons and InLens detectors with a 10 keV accelerating voltage and a 0.8 nA current.

Electrochemistry

The synthesized $NaNb_7O_{18}$ was mixed with binder and carbon in an 8:1:1 ratio. N-methyl-2-pyrrolidone (NMP) solvent was added to the mixture to form a thick slurry, which was cast on Cu foil. After drying in a vacuum furnace, 10 mm electrodes were punched and assembled into coin cells. The conductive carbon employed was TIMCAL SuperP and the binder was polyvinylidene fluoride (Kynar 2800). The cast foils were punched into 10 mm disk electrodes. The typical loading of active materials on the electrodes were between 3 and $4 \, mg \, cm^{-2}$. Coin cells (MTI parts, 2032 SS casings) were assembled from the electrodes in an argon-filled glove box using polished Li foil (Sigma Aldrich) as the counter electrode, and 16 mm glass fiber separators (Whatman GF/D), and $1 \, M \, LiPF_6$ EC:DMC electrolyte (Sigma Aldrich). Cells were crimped under 8 tons of pressure. Electrochemistry experiments were performed on the assembled coin cells using a BioLogic potentiostat VMP 3 (EC-Lab v11.43) at $25 \, °C$ in a controlled environment. To test extended

cycling performance, galvanostatic cycling was performed at a cycling rate of 2C between 1 V and 3 V for 200 cycles with a 5-minute rest interval between cycles. For variable rate cycling, cycling rates of C/10, C/5, 1C, 2C, 5C, and 10C were used, each for 5 cycles. C rates were calculated based on one Li per transition metal and a theoretical capacity of 195.1 mAh g^{-1}.

Inductively Coupled Plasma Atomic Emission Spectroscopy

To better understand the stability of the NaNb$_7$O$_{18}$ structure, the Na:Nb ratio was characterized by Inductively Coupled Plasma Atomic Emission Spectroscopy (ICP-OES Agilent 5800). Three samples were created from cathode casts: a 'pristine' sample that was only cast, a 'rested' sample that was assembled into a coin cell but never cycled, and a 'cycled' sample that was assembled into a coin cell and cycled. To prepare samples, active material ($\approx$8 mg) was scrapped from the copper current collector and washed 3 times in 5 cm^3 of acetone to remove the PVDF binder. Samples were digested in 1 cm^3 of HF/HNO$_3$ (50:50 by volume, Fisher Scientific, Trace Metals Grade). Conductive carbon was removed from the digestions through centrifugal action after dilution. Certified Na and Nb standards (Inorganic Ventures) were used to create a calibration curve with relative standard error values below 3% and correlation coefficients above 0.99999. Relatiove standard deviation values for all samples fell below 1

Potentiometric entropy measurements

The potentiometric entropy measurement technique was performed on coin cells with NaNb$_7$O$_{18}$ working electrodes and Li metal counter electrodes, using the setup described previously.[21,28,29] Specifically, the open-circuit voltage $U_{OCV}(x,T)$ and entropic potential $\partial U_{OCV}(x,T)/\partial T$ of coin cells were measured as functions of Li composition x. Over the measurements at 20°C, a series of 30 minute constant current pulses corresponding to

C/10 were imposed, each followed by a relaxation period (270 min). During the relaxation periods, a step-like temperature profile was applied to the coin cell from 15°C to 25°C in 5°C increments with a thermo-electric cold plate (TE technology, CP-121). Simultaneously, the corresponding coin cell potential evolution was recorded with a potentiostat (BioLogic, VSP-300). Near the end of every temperature step, it was verified that the coin cell had reached thermodynamic equilibrium if (i) the temperature difference between the cold plate and the top of the coin cell was less than 0.1°C and (ii) the time rate of change of the open-circuit voltage $\partial U_{OCV}(x, T)/\partial t$ was less than $1 \, mV \, h^{-1}$.

Results and discussion
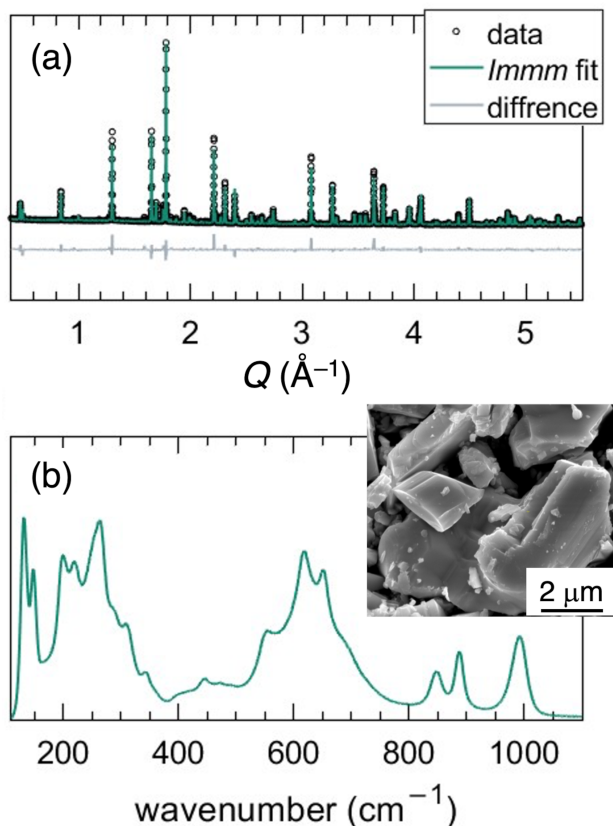
Figure 1: (a) Rietveld refinement of powder X-ray diffraction data and (b) Raman spectrum collected on $NaNb_7O_{18}$ powder. The inset displays an SEM image of an as-prepared powder.

9

NaNb$_7$O$_{18}$ powders were prepared from ceramic synthesis and characterized by powder synchrotron X-ray diffraction and Raman spectroscopy, as presented in Figure 1. Rietveld refinement of using the TOPAS suite of programs[26] shows a single-phase fit to the reported *Immm* structure, with structural details presented in the Supporting Information section. The phase diagram of Na$_2$O and Nb$_2$O$_5$ suggests that other stable compositions could result from this synthesis.[30] We therefore employed Raman spectroscopy as a complementary method to X-ray diffraction. Figure 1(b) shows Raman peaks at 131.0, 147.8, 199.7, 219.9, 263.9, 307.6, 343.7, 446.6, 553.78, 618.4, 650.14, 847.3, 886.74, and 990.9 cm^{-1}. We can establish that the spectrum is consistent with the refined structure and composition on the basis for prior studies on a series of niobium oxide reference compounds.[31–35] The low-frequency peaks (last three) represent different Nb–O longitudinal vibration modes, where 990 cm^{-1} is associated with corner-sharing oxygen and the other two (847.3 cm^{-1}, 886.74 cm^{-1}) with two different environments of the edge-sharing Nb-O bonds. Peaks in the 600 to 660 cm^{-1} range are related to Nb–O transverse vibrational modes. The 550 cm^{-1} peak is associated with the block structure. The higher frequency (210 to 350 cm^{-1}) peaks are associated with asymmetric octahedra resulting from disorder, and therefore, these peaks are broad. The peaks below 200 cm^{-1} are assigned to metal-metal bonds. Both the X-ray diffraction and Raman spectroscopy show a good fit with the literature, indicating that we synthesized a pure compound. Scanning electron microscopy (SEM) on the bulk powder particles is shown as a inset, and reveals highly crystalline particles about 1 μm to 5 μm in size.

Figure 2(a) shows projections of the structure of NaNb$_7$O$_{18}$. This structure has 4×4 ReO$_3$ blocks tiled in a zig-zag pattern with crystallographic shear at the edges. Each unit cell contains sodium located at the edges of blocks, in channels that are not accessible to Li–ions. Figure 2(b) shows the diffusion landscape of Li–ions calculated using the bond-valence sum (BVS) method[36] using the SoftBV code.[37,38] The isosurface was set to $\delta\nu = 0.1$ where $\delta\nu$ is indicative of the half-width (in valence units) of the volume accessible
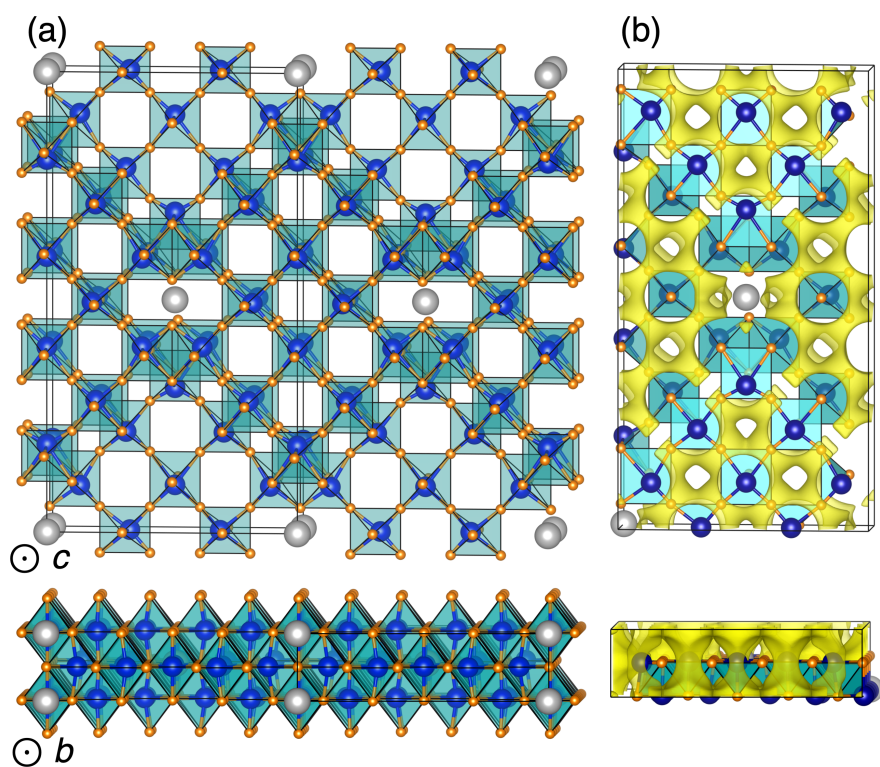
Figure 2: (a) Projections of the crystal structure of $NaNb_7O_{18}$ and (b) Li^+- valence bond map for an isosurface with $\Delta\nu = 0.1$ valence units created using softBV, showing connected pathways for high Li^+ diffusion in all directions of the crystal structure.

to the mobile ion. The connected isosurface indicates low energy barriers for intra-block hopping in the $a - b$ plane and also low energy pathways along the c axis within the blocks. A value of $\delta\nu = 0.1$ is highly suggestive of low migration barriers, an usually corresponds to a barrier height of less that 200 meV. These multiple channels for Li–ion transport are continuous pathways and consistent with similar Wadsley-Roth Li- ion transport. A similar analysis for Na–ions within this compound suggests that Na-ion can occupy the channels but cannot hop along the c axis (down channels) or within the $a - b$ plane due to high migration barriers.

The electrochemical performance of NaNb$_7$O$_{18}$ was tested in a half-cell configuration *vs.* Li metal, and is presented in the four panels of Figure 3. Panel (a) shows the charging and discharging profiles of different galvanostatic cycling rates. At a low rates, the compound can store 175 mAh g^{-1}. The observed value is slightly lower than the theoretical 1-electron capacity *per* Nb which is 195 mAh g^{-1}, perhaps due to the large particle size, and due to Li transport bottlenecks near the Na sites in the structure as seen in Figure 2. Smaller particles that could be prepared by ball milling or by soft-chemical synthesis can be considered as a means for demonstrating higher capacities in this compound, as seen in other studies of Wadsley-Roth electrodes.[39–41] Panel (b) shows the derivative of the charge as a function of the voltage, dQ/dV. This highlights the Nb redox peaks along the reaction path. There are two intense peaks between 1.65 V to 1.55 V and another smaller peak at 1.4 V. The capacity associated with these sharp peaks is the representation of phase transition around the redox voltage of the niobium during each lithiation and delithiation. It provides evidence that a large fraction of the reaction is a two-phase reaction when applying a slow galvanostatic cycle because the sharp peak results from a constant voltage as long as the two phases coexist. For a higher cycling rate, the two-phase reaction (plateau in the $I - V$ curve) is smaller, though a substantial capacity is still stored at those rates.

To verify that Na in the electrodes is not exchanged with Li or otherwise contributing to the electrochemistry, we have carried out Inductively Coupled Plasma – Atomic Emission
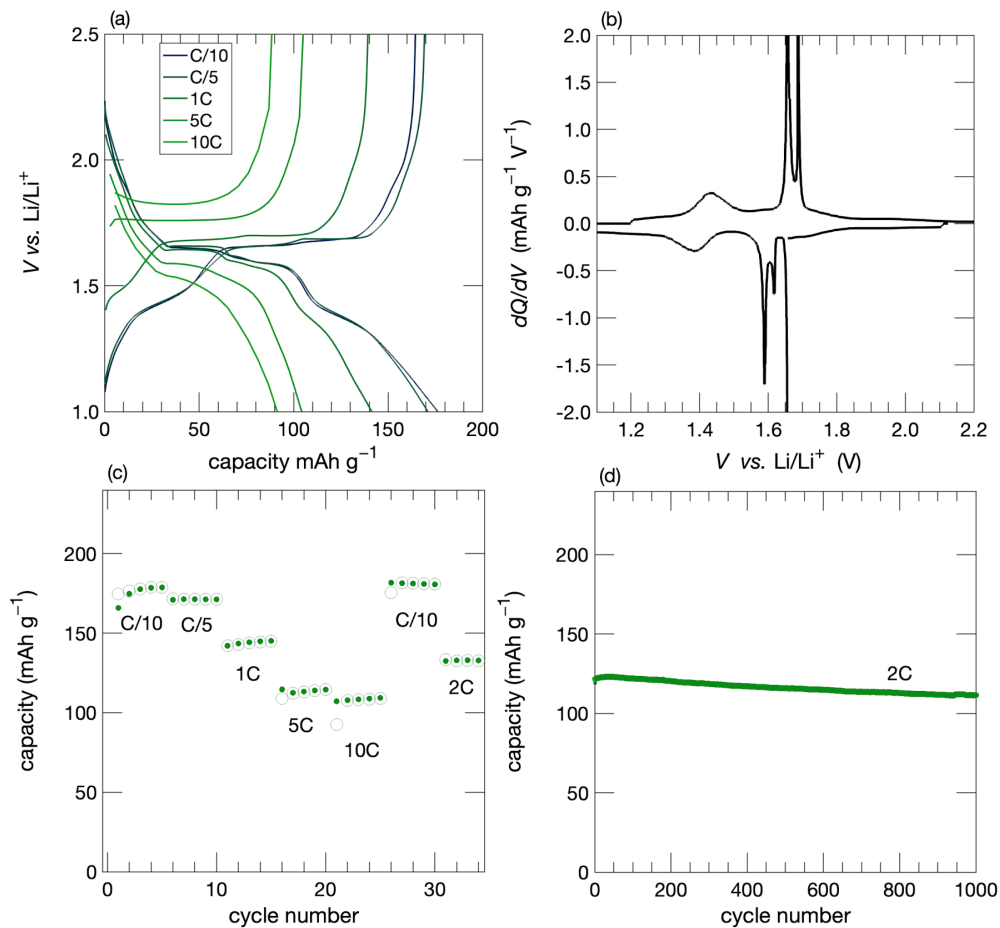
Figure 3: (a) Charging and discharging profile of $NaNb_7O_{18}$ anode *vs.* Li metal at C/10, C/5, 1C, 5C and 10C rates between 1 V and 3.0 V (where 1C = $0.195\,A\,g^{-1}$). (b) dQ/dV as a function of the voltage of the first cycle at C/10 rate. (c) Variable rate galvanostatic cycling rates from C/10 to 10C. Open circles represent charging capacity and the closed circles are discharging capacity. (d) Long-term galvanostatic with good capacity retention at 2C ($\geq$ 90%).

Spectrometry (ICP-AES) spectroscopy with standards, for pristine $NaNb_7O_{18}$, $NaNb_7O_{18}$ after resting in cells for 24 h, and after two weeks of cycling at a 2C rate, with the electrode dissolved in aqua regia and diluted appropriately. The expected elemental ratio of Na:Nb is 1:7 or 0.143. The as-prepared sample was measured to have the Na:Nb ratio 0.141. The samples that were rested in cells and cycled respectively measured 0.171 and 0.167, suggesting no Na loss. This supports the bond valence analysis suggests that Na in the structure is not mobile.

The capacity measurements of $NaNb_7O_{18}$ at high rates and long-term cycling at 2C (30 minutes for charging or discharging) were performed as illustrated in Figure 3(c) and 3(d), and can bring insight regarding the Li–ion kinetics in two-phase reactions. At high rates, $NaNb_7O_{18}$ half cell can charge up to $95\,\mathrm{mAh\,g^{-1}}$ in 6 min. This despite the relatively large particle sizes noted, on the order of $1\,\mu m$ to $5\,\mu m$. The long-term cycling of the half cell at 2C show that 90% of its original capacity is retained after 1000 cycles ($111\,\mathrm{mAh\,g^{-1}}$ versus initial capacity of $121\,\mathrm{mAh\,g^{-1}}$). The capacity retention hints that the material does not have significant structural change or decomposition during those reactions. Two reasons can explain these remarkable results: (i) the electrochemical reaction voltage window does not involve the decomposition of any of the compounds in the cell, including the electrolyte and the additives, and hence, prevents SEI formation on this anode. (ii) the Wadsley-Roth material contains open Li–ion channels and a shear structure that forms a stable framework even when a large number of ions leave the structure and ensures long-term cyclability.
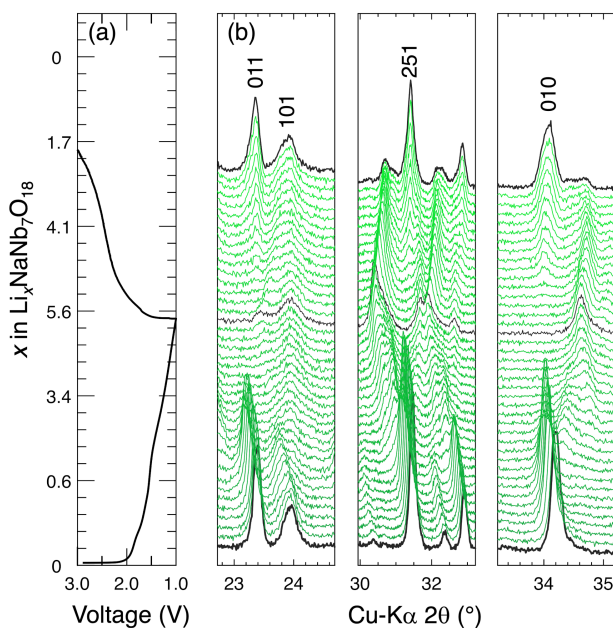

Figure 4: *Operando* XRD of $NaNb_7O_{18}$ discharged to $1.0\,\mathrm{V}$ and charged to $3.0\,\mathrm{V}$ at a C/10 rate. Panel (a) displays electrochemical data and the three panels (b) display select diffraction peaks.

The structural evolution during Li insertion were observed by *operando* X-ray diffraction using a custom cell with a Be window. Figure 4 shows the first charge and discharge cycle at a C/10 rate. Panel (a) presents galvanostatic measurement as a function of x in $Li_xNaNb_7O_{18}$. The three right panels (b) show the diffraction patterns for selected peaks (the complete data is available in SI), starting with the pristine electrode at the bottom and stacking up along the electrochemical reaction, recorded in the panel (a). The pristine $NaNb_7O_{18}$ X-ray diffraction displayed a pure phase, and the peaks gradually migrate to lower angles as Li–ions are inserted into the structure during the charging step. Much of the volume expansion seems associated with an expansion in the b cell parameter, which corresponds to the long direction of the channels that contain Na^+. After the first plateau at about 1.6 V, the diffraction intensity decreases, and a new phase starts appearing. When a phase transition occurs, the symmetry of the structure appears to remain the same with a contraction of the $a - b$ plane and expansion along c. Lattice contraction in the block unit and layer expansion along c are commonly observed in other Wadsley-Roth compounds during Li intercalation[42] due to metal-metal bond formation along the edges of the blocks in these structure. The expansion along c potentially accommodates the additional Li–ion volume.

During discharge, a recovery of the original phase position can be observed as it slowly forms and shows a peak intensity and shape similar to that of the pristine material. A few new peaks with low intensity still appear in the fully discharged diffraction (the top line), which could be explained by the low Coulombic efficiency when using the *operando* cell with limited performance. The electrochemical data suggests that some Li remaining in the structure, which is not observed when coin cells are prepared. Generally, based on the peak intensities and shapes after a full cycle, the same phase is obtained, and the volume expansion during the lithiation is minimal. Future measurements using a high-intensity light source can accurately determine the volume change as a function of Li–ion insertion. Those measurements have been applied for other Wadsley-Roth material members that

15

presented less than 10% volume expansion, such as $W_3Nb_{14}O_{44}$ with a total volume change of about 5.9%, $LiScMo_3O_8$ shows 3%,[43] and for $TiNb_2O_7$ with 7.22%.[44]
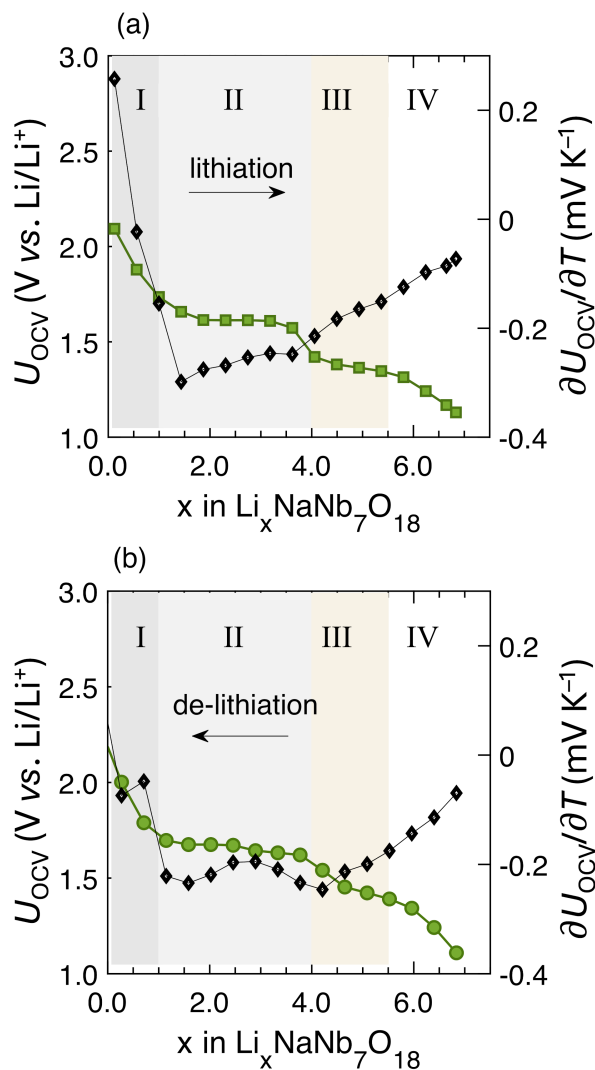

Figure 5: Potentiometric entropy measurements of $NaNb_7O_{18}$ *vs.* Li. The open-circuit voltage $U_{OCV}(x)$ and the entropic potential $\partial U_{OCV}(x)/\partial T$ as functions of Li composition x are displayed during (a) lithiation and (b) delithiation cycling at C/10 rate at 20° C
.

$NaNb_7O_{18}$ is clearly a promising candidate for fast-charging electrodes based on the electrochemical data that show small capacity loss between 2C, 5C, and 10C during charging along with minimal structural changes after a full cycle. To learn about the charge storage mechanisms in the structure, we performed potentiometric entropy measurements, which determined the open-circuit voltage $U_{OCV}(x,T)$ and the entropic potential $\partial U_{OCV}(x,T)/\partial T$.

16

Both $U_{OCV}(x,T)$ and $\partial U_{OCV}(x,T)/\partial T$ relate to fundamental thermodynamic quantities of the electrodes according to the Nernst equation and Gibbs energy law.[21] Figure 5 shows the open-circuit voltage $U_{OCV}(x,T)$ and the entropic potential $\partial U_{OCV}(x,T)/\partial T$ during (a) lithiation and (b) delithiation. We can identify four different regions. First, in Region I ($0 \leq x < 1.0$), both $U_{OCV}(x,T)$ and $\partial U_{OCV}(x,T)/\partial T$ decrease sharply with increasing x corresponding to Li insertion in a homogeneous solid solution.[21] In Region II ($1.0 \leq x < 4.0$, $U_{OCV}(x,T)$ features a plateau indicating the first two-phase coexistence.[21] Interestingly, in particular during delithiation, $\partial U_{OCV}(x,T)/\partial T$ shows a tilde-shaped fluctuation typically associated with intralayer ion ordering.[21] Therefore, we hypothesize that while the structure undergoes two-phase reactions, intralayer ion ordering also occurs within either or both of the two phases. This feature could also play a role in the high rate performance, which is consistent with our previous studies on other Wadsley-Roth structure materials with ion ordering and generally demonstrating outstanding fast charging capability.[21,28] Similarly, in Region III ($4.0 \leq x < 5.5$), another plateau in $U_{OCV}(x,T)$ is observed, indicating the second two-phase coexistence.[21] In addition, $\partial U_{OCV}(x,T)/\partial T$ showed another tilde-shaped fluctuation, albeit not as visible as in Region II, with the continued presence of intralayer ion ordering.[21] Finally, in Region IV ($5.5 \leq x < 7.0$, $U_{OCV}(x,T)$ decreased monotonously while $\partial U_{OCV}(x)/\partial T$ increased monotonously, which is also characteristic of Li insertion in a homogeneous solid solution.[21] Overall, all the features above were repeatable between lithiation and delithiation as the material cycled reversibly. Furthermore, within Regions II and III, the potentials where the two-phase reactions took place were consistent with those observed from *operando* XRD. It should be noted that, compared to the cases from previous studies,[21,28] the magnitude of the tilde-shaped fluctuation in $\partial U_{OCV}(x)/\partial T$ was relatively small. This reflects a minimal difference between the energies of the various sublattice sites.[21] Thus, the migration barriers for Li insertion at different sublattice sites should be very low. Therefore, this would lead to the case of two-phase reactions with a low preference for site occupation.
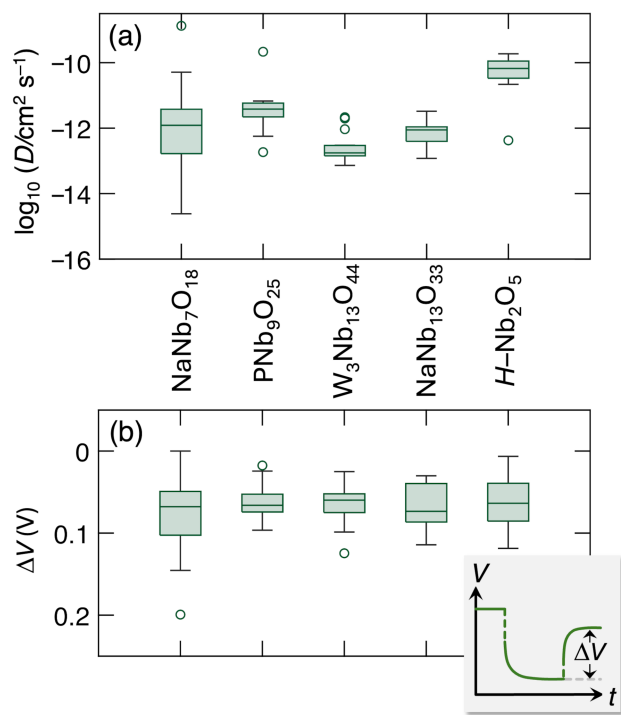
Figure 6: (a) Diffusion coefficient $\log_{10}(D)$ and (b) overpotential ΔV during the charging process for different shear-structures Nb–oxide anode materials. The box represents less than $\pm 1\sigma$ and the open circles are the outliers ($> \pm 3\sigma$). Individual GITT measurements can be found in the SI.

The results obtained on $NaNb_7O_{18}$ encourage us to broaden our conclusion by looking at two kinetics parameters for five different Wadsley-Roth compounds. The ion diffusion coefficient (D) is a key parameter in the literature that quantifies the ion transport in solids. The conventional way to find D is to apply Fick's second law. The concentration of ions can be challenging to measure in a closed system such as a cell. GITT is often used to extract the apparent diffusion coefficient by measuring the voltage profile during a sequence of current pulses followed by rest periods.[19,45] The measured voltage can be converted to concentration using the Nernst equation and plugged back into Fick's second law. This can be true as long as the voltage represents the changes in ion concentration. As discussed in the introduction, the reaction occurs in a few ways. For a pure two-phase reaction, the voltage stays constant until the new phase is formed and ion transport is not Fickian. Hence, the true diffusion coefficient cannot be extracted from GITT (or other impedance techniques) during a pure two-phase reaction. However, the two-phase reaction is only part of the Li insertion process, and we can use the other parts of the reaction to learn about the diffusion behavior. Figure 6(a) summarizes in a box plot, the diffusion coefficients during Li–ion insertion for $NaNb_7O_{18}$ and four other Wadsley-Roth compounds made by solid-state synthesis (see SI). Those anodes were cycled using the GITT methods, where the current pulse was set to a C/20 rate followed by 3 hours of relaxation between each current pulse. The open-circuit voltage was recorded and used later for further analysis of the overpotential. The box represents less than $\pm 1\sigma$ and the open circlets are the outliers that differ significantly from the rest of the dataset ($> \pm 3\sigma$).

The data collected by GITT can be used to calculate the overpotential of Li insertion, representing the energy of adding/removing ions to/from the structure. The overpotential is calculated from the voltage gap between the end of the current pulse step and the open voltage circuit after the system relaxes to an equilibrium [Figure 6(b)]. The larger this value, the higher the energy required for Li insertion into a compound. Similar to the diffusion coefficient, there is only a small variation between the compounds. The materials

are ordered from the least sloped I–V curve to the most sloped curve. A sloped curve represents a solid solution process, and flat regions (plateaux) correspond to a two-phase reaction. The measured diffusion values are between 10^{-14} and 10^{-10} $cm^2\,sec^{-1}$ for all five compounds with no clear trend of whether the GITT are sloped or show flat regions.

In conclusion, $NaNb_7O_{18}$ has been established as a member of the Wadsley-Roth family of oxide compounds that is extremely effective as a fast-charging anode for Li–ion batteries, with exceptional performance, including capacity retention even after 1000 cycles. Given the relatively elevated anode voltage, we anticipate that when this material is coupled with a high-voltage cathode, acceptable full-cell energy densities can be accessed. This compound is highly ordered, and Li insertion takes place mainly through two-phase reactions, which is somewhat surprising for a material displaying fast charging. Potentiometric entropy measurements confirm two-phase reactions as the primary charge storage mechanism. They also provide evidence for intralayer ion ordering. In addition, we have shown that low migration barriers between different Li sites result in fast Li–ion insertion (within minutes rather than hours). The diffusion coefficients and overpotentials for other Wadsley-Roth members were found to be similar, showing that the type of reaction during intercalation does not appear to influence the kinetics. Low migration barriers are clearly the essential feature for fast insertion in electrode materials, and we believe this arises from rigid channels for Li–ion transport in the structure — consistent with the structural symmetry being conserved, with only small changes in unit cell parameters.

Supporting Information

Table describing the results of Rietveld refinement of synchrotron X-ray diffraction on $NaNb_7O_{18}$, bond valence analysis for Na–ion transport compared with Li–ion transport in $NaNb_7O_{18}$, complete *operando* X-ray diffraction on $NaNb_7O_{18}$ as a function of Li insertion, GITT plots for Li insertion for all five compounds (along with their preparation) that

are discussed in Figure 6.

Acknowledgements

References

(1) Kang, K.; Meng, Y. S.; Bréger, J.; Grey, C. P.; Ceder, G. Electrodes with High Power and High Capacity for Rechargeable Lithium Batteries. *Science* **2006**, *311*, 977–980.

(2) Roberts, M. R.; Madsen, A.; Nicklin, C.; Rawle, J.; Palmer, M. G.; Owen, J. R.; Hector, A. L. Direct Observation of Active Material Concentration Gradients and Crystallinity Breakdown in $LiFePO_4$ Electrodes During Charge/Discharge Cycling of Lithium Batteries. *J. Phys. Chem.* **2014**, *118*, 6548–6557.

(3) Xu, C.; Märker, K.; Lee, J.; Mahadevegowda, A.; Reeves, P. J.; Day, S. J.; Groh, M. F.; Emge, S. P.; Ducati, C.; Mehdi, B. L.; Tang, C. C.; Grey, C. P. Bulk Fatigue Induced by Surface Reconstruction in Layered Ni-Rich Cathodes for Li-Ion Batteries. *Nat. Mater.* **2021**, *20*, 84–92.

(4) Simon, B.; Flandrois, S.; Guerin, K.; Fevrier-Bouvier, A.; Teulat, I.; Biensan, P. On the Choice of Graphite for Lithium Ion Batteries. *J. Power Sources* **1999**, *81*, 312–316.

(5) An, S. J.; Li, J.; Daniel, C.; Mohanty, D.; Nagpure, S.; Wood III, D. L. The State of Understanding of the Lithium-Ion-Battery Graphite Solid Electrolyte Interphase (SEI) and its Relationship to Formation Cycling. *Carbon* **2016**, *105*, 52–76.

(6) Verma, P.; Maire, P.; Novák, P. A Review of the Features and Analyses of the Solid Electrolyte Interphase in Li-Ion Batteries. *Electrochim. Acta* **2010**, *55*, 6332–6341.

(7) Wang, Y.; Guo, X.; Greenbaum, S.; Liu, J.; Amine, K. Solid Electrolyte Interphase Formation on Lithium-Ion Electrodes: A [7]Li Nuclear Magnetic Resonance Study. *Electrochem. Solid State Lett.* **2001**, *4*, A68.

(8) Griffith, K. J.; Harada, Y.; Egusa, S.; Ribas, R. M.; Monteiro, R. S.; Von Dreele, R. B.; Cheetham, A. K.; Cava, R. J.; Grey, C. P.; Goodenough, J. B. Titanium Niobium Oxide:

From Discovery to Application in Fast-Charging Lithium-Ion Batteries. *Chem. Mater.* **2020**, *33*, 4–18.

(9) Wang, M.; Yao, Z.; Li, Q.; Hu, Y.; Yin, X.; Chen, A.; Lu, X.; Zhang, J.; Zhao, Y. Fast and Extensive Intercalation Chemistry in Wadsley-Roth Phase Based High-Capacity Electrodes. *J. Energy Chem.* **2022**, *69*, 601–611.

(10) Xie, F.; Xu, J.; Liao, Q.; Zhang, Q.; Liu, B.; Shao, L.; Cai, J.; Shi, X.; Sun, Z.; Wong, C.-P. Progress in Niobium-Based Oxides as Anode for Fast-Charging Li-Ion Batteries. *Energy Rev.* **2023**, *2*, 100027.

(11) Voskanyan, A. A.; Navrotsky, A. Shear Pleasure: The Structure, Formation, and Thermodynamics of Crystallographic Shear Phases. *Annu Rev. Mater. Res.* **2021**, *51*, 521–540.

(12) Preefer, M. B.; Saber, M.; Wei, Q.; Bashian, N. H.; Bocarsly, J. D.; Zhang, W.; Lee, G.; Milam-Guerrero, J.; Howard, E. S.; Vincent, R. C.; others Multielectron Redox and Insulator-to-Metal Transition upon Lithium Insertion in the Fast-Charging, Wadsley-Roth Phase PNb_9O_{25}. *Chem. Mater* **2020**, *32*, 4553–4563.

(13) Radin, M. D.; Van der Ven, A. Simulating Charge, Spin, and Orbital Ordering: Application to Jahn–Teller Distortions in Layered Transition-Metal oxides. *Chem. Mater* **2018**, *30*, 607–618.

(14) Bhattacharya, J.; Van der Ven, A. Phase Stability and Nondilute Li Diffusion in Spinel $Li_{1+x}Ti_2O_4$. *Phys. Rev. B.* **2010**, *81*, 104304.

(15) Belak, A. A.; Wang, Y.; Van der Ven, A. Kinetics of Anatase Electrodes: the Role of Ordering, Anisotropy, and Shape Memory Effects. *Chem. Mater* **2012**, *24*, 2894–2898.

(16) Griffith, K. J.; Wiaderek, K. M.; Cibin, G.; Marbella, L. E.; Grey, C. P. Niobium Tungsten Oxides for High-Rate Lithium-Ion Energy Storage. *Nature* **2018**, *559*, 556–563.

(17) Yang, Y.; Zhao, J. Wadsley–Roth Crystallographic Shear Structure Niobium-Based oxides: Promising Anode Materials for High-Safety Lithium-Ion Batteries. *Adv. Sci.* **2021**, *8*, 2004855.

(18) Patterson, A. R.; Elizalde-Segovia, R.; Wyckoff, K. E.; Zohar, A.; Ding, P. P.; Turner, W. M.; Poeppelmeier, K. R.; Narayan, S. R.; Clément, R. J.; Seshadri, R.; Griffith, K. J. Rapid and Reversible Lithium Insertion in the Wadsley–Roth-Derived Phase $NaNb_{13}O_{33}$. *Chem. Mater.* **2023**, *35*, 6364–6373.

(19) Van der Ven, A.; Bhattacharya, J.; Belak, A. A. Understanding Li Diffusion in Li-Intercalation Compounds. *Acc. Chem. Res.* **2013**, *46*, 1216–1225.

(20) Koçer, C. P.; Griffith, K. J.; Grey, C. P.; Morris, A. J. Cation Disorder and Lithium Insertion Mechanism of Wadsley-Roth Crystallographic Shear Phases from First Principles. *J. Am. Chem. Soc.* **2019**, *141*, 15121–15134.

(21) Baek, S. W.; Saber, M.; Van der Ven, A.; Pilon, L. Thermodynamic Analysis and Interpretative Guide to Entropic Potential Measurements of Lithium-Ion Battery Electrodes. *J. Phys. Chem. C* **2022**, *126*, 6096–6110.

(22) Clément, R.; Lun, Z.; Ceder, G. Cation-Disordered Rocksalt Transition Metal Oxides and Oxyfluorides for High Energy Lithium-Ion Cathodes. *Energy & Env. Sci.* **2020**, *13*, 345–373.

(23) Marinder, B.-O.; Sundberg, M. The Structure of $NaNb_7O_{18}$ as Deduced from HREM Images and X-ray Powder Diffraction Data. *Acta Crystallogr. B* **1984**, *40*, 82–86.

(24) Deiss, E. Spurious Chemical Diffusion Coefficients of Li^+ in Electrode Materials Evaluated with GITT. *Electrochim. Acta* **2005**, *50*, 2927–2932.

(25) Kim, J.; Park, S.; Hwang, S.; Yoon, W.-S. Principles and Applications of Galvanostatic Intermittent Titration Technique for Lithium-Ion Batteries. *J. Electrochem. Sci. Technol.* **2022**, *13*, 19–31.

(26) Coelho, A. A. TOPAS and TOPAS-Academic: An Optimization Program Integrating Computer Algebra and Crystallographic Objects Written in C++. *J. Appl. Crystallogr.* **2018**, *51*, 210–218.

(27) Momma, K.; Izumi, F. *VESTA 3* for Three-Dimensional Visualization of Crystal, Volumetric and Morphology Data. *J. Appl. Crystallogr.* **2011**, *44*, 1272–1276.

(28) Baek, S. W.; Wyckoff, K. E.; Butts, D. M.; Bienz, J.; Likitchatchawankun, A.; Preefer, M. B.; Frajnkovič, M.; Dunn, B. S.; Seshadri, R.; Pilon, L. *Operando* Calorimetry Informs the Origin of Rapid Rate Performance in Microwave-prepared $TiNb_2O_7$ Electrodes. *J. Power Sources* **2021**, *490*, 229537.

(29) Zhou, Y.; Luo, Y.; Patterson, A.; Baek, S. W.; Frajnkovič, M.; Seshadri, R.; Dunn, B. S.; Pilon, L. Microcalorimetry Electrothermal Impedance Spectroscopy (ETIS) Informs Entropy Evolution at Individual Electrodes of PNb_9O_{25} or $TiNb_2O_7$ Battery Cells. *Electrochim. Acta* **2023**, *468*, 143072.

(30) Shafer, M.; Roy, R. Phase Equilibria in the System Na_2O–Nb_2O_5. *J. Am. Ceram. Soc.* **1959**, *42*, 482–486.

(31) McCarroll, W. H.; Katz, L.; Ward, R. Some Ternary Oxides of Tetravalent Molybdenum. *J. Am. Chem. Soc.* **1957**, *79*, 5410–5414.

(32) Hardcastle, F. D.; Wachs, I. E. Determination of Niobium-Oxygen Bond Distances and Bond Orders by Raman Spectroscopy. *Solid State Ionics* **1991**, *45*, 201–213.

(33) Huang, B. X.; Wang, K.; Church, J. S.; Li, Y.-S. Characterization of Oxides on Niobium by Raman and Infrared Spectroscopy. *Electrochimica acta* **1999**, *44*, 2571–2577.

(34) Pittman, R. M.; Bell, A. T. Raman Studies of the Structure of Niobium Oxide/Titanium Oxide ($Nb_2O_5.TiO_2$). *J. Phys. Chem.* **1993**, *97*, 12178–12185.

(35) Han, J. T.; Huang, Y. H.; Goodenough, J. B. New Anode Framework for Rechargeable Lithium Batteries. *Chem. Mater.* **2011**, *23*, 2027–2029.

(36) Brown, I. D. Recent Developments in the Methods and Applications of the Bond Valence Model. *Chem. Rev.* **2009**, *109*, 6858–6919.

(37) Chen, H.; Wong, L. L.; Adams, S. SoftBV–A Software Tool for Screening the Materials Genome of Inorganic Fast Ion Conductors. *Acta Cryst. B. Struct. Sci. Cryst. Eng. Mater.* **2019**, *75*, 18–33.

(38) Wong, L. L.; Phuah, K. C.; Dai, R.; Chen, H.; Chew, W. S.; Adams, S. Bond Valence Pathway Analyzer—An Automatic Rapid Screening Tool for Fast Ion Conductors within softBV. *Chem. Mater.* **2021**, *33*, 625–641.

(39) Wyckoff, K. E.; Robertson, D. D.; Preefer, M. B.; Teicher, S. M.; Bienz, J.; Kautzsch, L.; Mates, T. E.; Cooley, J. A.; Tolbert, S. H.; Seshadri, R. High-Capacity Li^+ Storage through Multielectron Redox in the Fast-Charging Wadsley–Roth phase $(W_{0.2}V_{0.8})_3O_7$. *Chem. Mater* **2020**, *32,* 9415–9424.

(40) Lou, S.; Cheng, X.; Gao, J.; Li, Q.; Wang, L.; Cao, Y.; Ma, Y.; Zuo, P.; Gao, Y.; Du, C.; Huo, H.; Yin, G. Pseudocapacitive Li^+ Intercalation in Porous $Ti_2Nbi_{10}O_{29}$ Nanospheres Enables Ultra-Fast Lithium Storage. *Energy Storage Mater.* **2018**, *11*, 57–66.

(41) Deng, Q.; Fu, Y.; Zhu, C.; Yu, Y. Niobium-Based Oxides Toward Advanced Electrochemical Energy Storage: Recent Advances and Challenges. *Small* **2019**, *15*, e1804884.

(42) Saber, M.; Preefer, M. B.; Kolli, S. K.; Zhang, W.; Laurita, G.; Dunn, B.; Seshadri, R.; Van der Ven, A. Role of Electronic Structure in Li Ordering and Chemical Strain in the Fast Charging Wadsley–Roth Phase PNb_9O_{25}. *Chem. Mater* **2021**, *33*, 7755–7766.

(43) Wyckoff, K. E.; Kaufman, J. L.; Baek, S. W.; Dolle, C.; Zak, J. J.; Bienz, J.; Kautzsch, L.; Vincent, R. C.; Zohar, A.; See, K. A.; Eggeler, Y. M.; Pilon, L.; Van der Ven, A.; Seshadri, R. Metal–Metal Bonding as an Electrode Design Principle in the Low-Strain Cluster Compound $LiScMo_3O_8$. *J. Am. Chem. Soc.* **2022**, *144*, 5841–5854.

(44) Yan, L.; Shu, J.; Li, C.; Cheng, X.; Zhu, H.; Yu, H.; Zhang, C.; Zheng, Y.; Xie, Y.; Guo, Z. $W_3Nb_{14}O_{44}$ nanowires: ultrastable lithium storage anode materials for advanced rechargeable batteries. *Energy Storage Mater.* **2019**, *16*, 535–544.

(45) Dees, D. W.; Kawauchi, S.; Abraham, D. P.; Prakash, J. Analysis of the Galvanostatic Intermittent Titration Technique (GITT) as Applied to a Lithium-Ion Porous Electrode. *J. Power Sources* **2009**, *189*, 263–268.

TOC Graphic
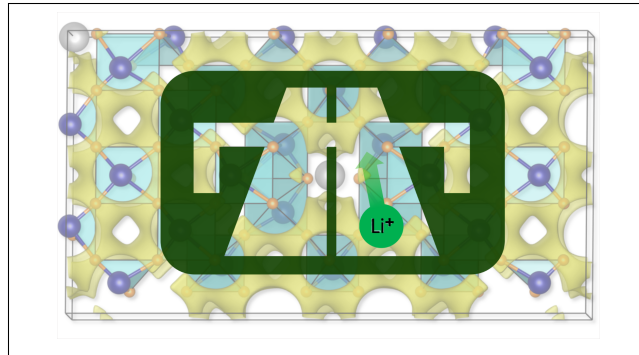
Supporting information for:

Fast Charging from Low Li–ion Migration Barriers in Wadsley-Roth NaNb₇O₁₈ Anodes

Arava Zohar,[†,‡] Tianyu Li,[†] Yucheng Zhou,[¶] Kira E. Wyckoff,[†] Alexander Justice Bologna,[§]
Ashlea Patterson,[†] Laurent Pilon,[¶] and Ram Seshadri[*,†,§]

†Materials Department and Materials Research Laboratory
University of California, Santa Barbara, California 93106, United States
‡Contributed equally to this work
¶Mechanical and Aerospace Engineering Department
Henry Samueli School of Engineering and Applied Science
University of California, Los Angeles, California 90095, United States
§Department of Chemistry and Biochemistry
University of California, Santa Barbara, California 93106, United States

E-mail: seshadri@mrl.ucsb.edu

NaNb$_7$O$_{18}$ refinement data:

R_{wp}=8.4 %

Space Group: *Immm*

a = 14.29109(6) Å; b = 26.2224(1); Å c = 3.84326(1) Å

| SITE	ATOM	X	Y	Z	OCC.	U_{ISO}
NA1	Na$^+$	0	0	0	1	0.057(7)
NB1	Nb^{5+}	0.1186(2)	0.1030(1)	0.5	1	0.0152(2)
NB2	Nb^{5+}	0.3059(2)	0.2072(1)	0.5	1	0.0152(2)
NB3	Nb^{5+}	0.3137(2)	0	0.5	1	0.0152(2)
NB4	Nb^{5+}	0	0.1889(1)	0	1	0.0152(2)
NB5	Nb^{5+}	0	0.3956(1)	0	1	0.0152(2)
O1	O^{2-}	0.702(1)	0.5540(5)	0	1	0.017(5)
O2	O^{2-}	0.900(1)	0.5509(5)	0	1	0.030(5)
O3	O^{2-}	0.7072(8)	0.6631(5)	0	1	0.002(4)
O4	O^{2-}	0.904(1)	0.6604(5)	0	1	0.027(3)
O5	O^{2-}	0.9016(8)	0.7700(4)	0	1	0.004(4)
O6	O^{2-}	0.101(1)	0.1202(5)	0	1	0.021(5)
O7	O^{2-}	0.2944(9)	0.2239(6)	0	1	0.020(5)
O8	O^{2-}	0	0.0607(7)	0.5	1	0.045(7)
O9	O^{2-}	0	0.1638(8)	0.5	1	0.032(7)
O10	O^{2-}	0	0.3868(8)	0.5	1	0.016(8)
O11	O^{2-}	0.307(1)	0	1	1	0.0158(4)
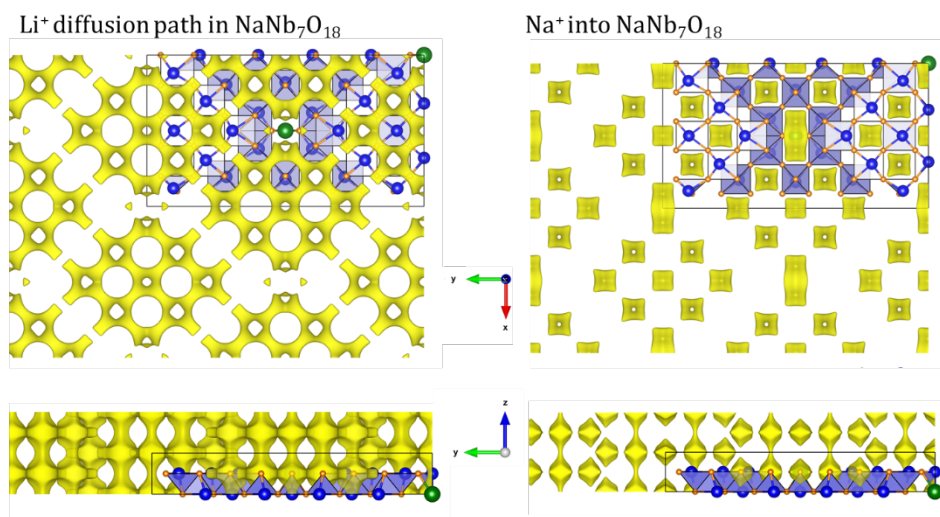
Figure S1: Li+ and Na+ valence bond map for an iso-surface with Δv = 0.1 valence units created using softBV, showing pathways for possible ion diffusion for Li$^+$ but much more limited for Na$^+$.
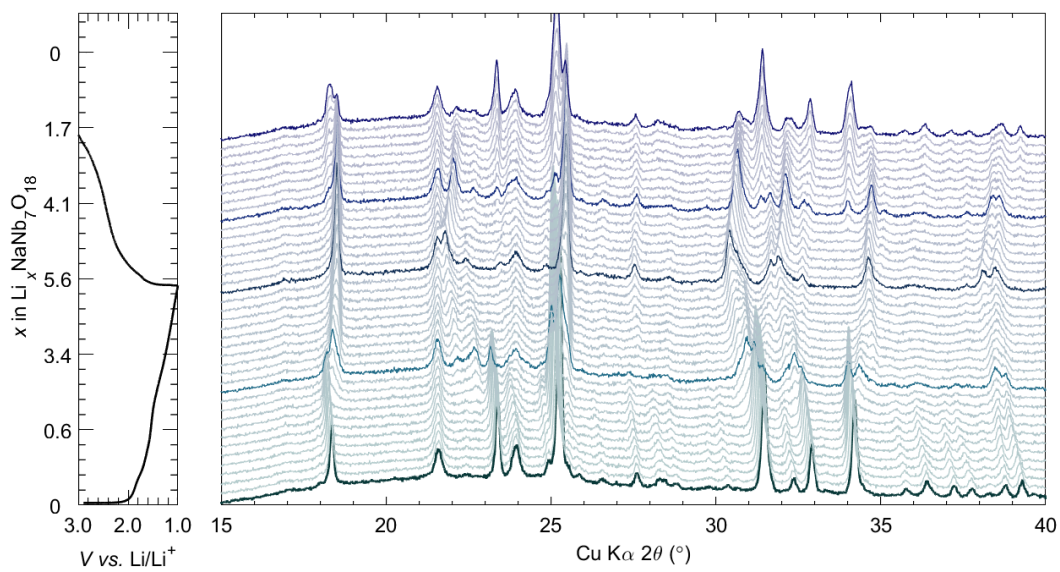

Figure S2: Operando XRD of NaNb$_7$O$_{18}$ discharged to 1 V and charged to 3.0 V at a C/10 rate.

Preparation of Compounds: The Wadsley-Roth compound for which data is presented in figure 6 were prepared by solid-state synthesis as follows.

$NaNb_7O_{18}$ and $NaNb_{13}O_{33}$: Both compounds contain a pre-step of forming $NaNbO_3$ from a stochiometric ratio of Nb_2O_5 (Materion, 99.95%) and Na_2CO_3 (Sigma, 99.95–100.05%, anhydrous). The mixture of the dried powders was pressed pellets and placed on Nb_2O_5 pellet in an alumina crucible, heated to 1100 °C for 12 h, and then air-quenched. To prepare powder Wadsley- Roth compound a stochiometric ratio of Nb_2O_5 (Materion, 99.95%) and $NaNbO_3$ were ground in an agate mortar for 10 minutes, pressed to pellets and placed into an alumina crucible into a furnace. The $NaNb_7O_{18}$ pellet was heated to 800°C for 24 hrs and then 1150°C for 48 hr. The $NaNb_{13}O_{33}$ pellet was headed to 400 °C for 6 hrs, 820 °C for 12 hrs, and 1150 °C for 18 hrs. Both samples were slowly cooled with at the furnace. $NaNb_{13}O_{33}$ is described in [1].

PNb_9O_{25}: A stoichiometric ratio of Nb_2O_5 (Materion, 99.95%) and $(NH_4)_3PO_4$ (Sigma-Aldrich, 98%), mixture and pressed into a pellet. Pellet was placed in an alumina crucible in air at 350°C for 20 hrs and at 1250 °C for 18 h. The sample were slowly cooled with at the furnace. Described in [2].

$W_3Nb_{13}O_{44}$: a stoichiometric ratio of Nb_2O_5 (Materion, 99.95%) and WO_3 (Sigma-Aldrich, 98%), mixture and pressed into a pellet. Pellet was placed in an alumina crucible in air at 350°C for 20 hrs and at 1250 °C for 18 h. The sample were slowly cooled with at the furnace.

$H-Nb_2O_5$: Nb_2O_5 (Materion, 99.95%) was pressed into a pellet, placed in an alumina crucible and heated in air at 1100°C for 18 hrs and then quenched into water.
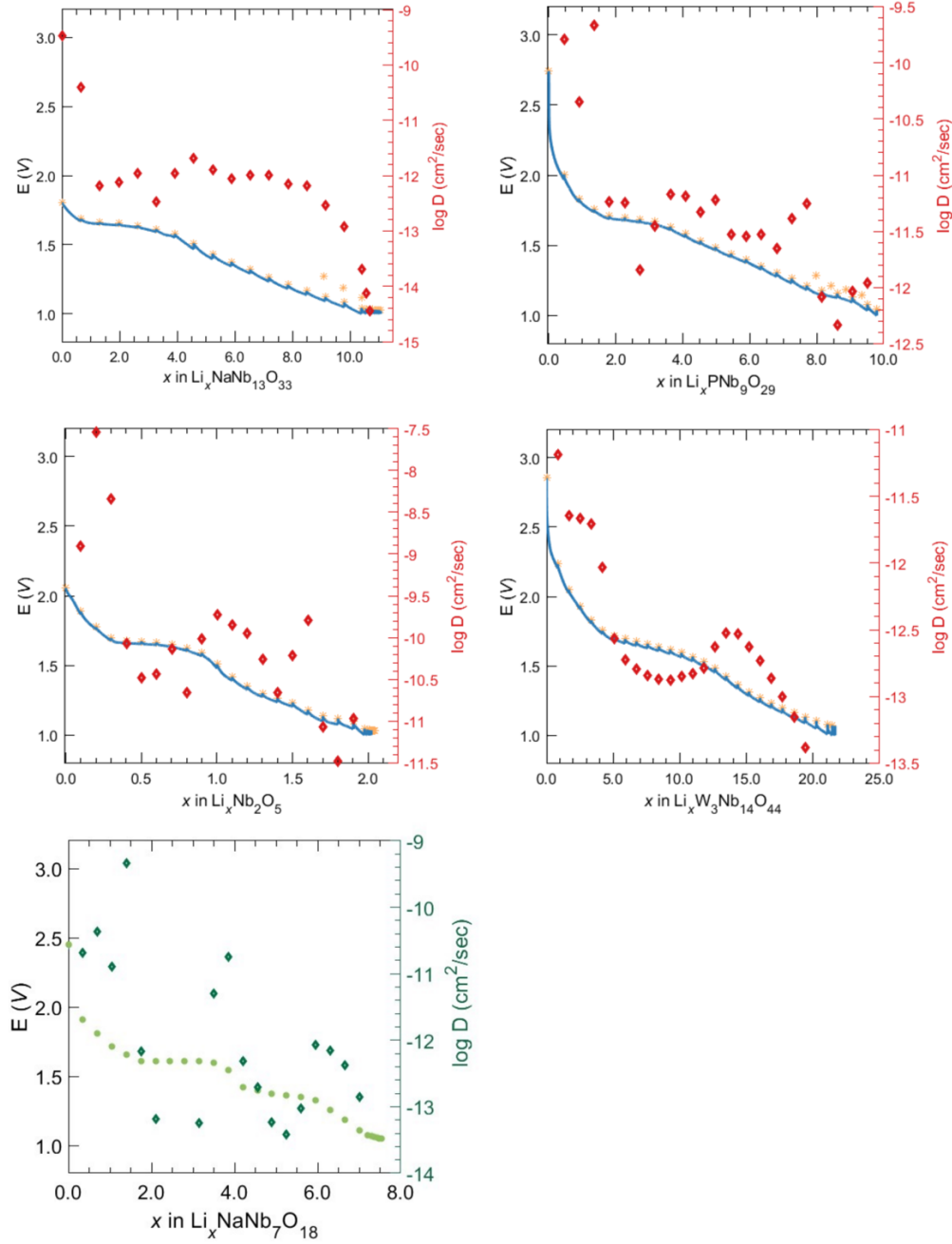
Figure S3- GITT measurements for $NaNb_{13}O_{33}$, PNb_9O_{25}, $H-Nb_2O_5$, $W_3Nb_{13}O_{44}$ and, $NaNb_7O_{18}$ compound. The charging rate was C/10 (blue line) for 1 hr following by 3 hrs rest time. The stars markers represent the open circuit voltage after the 3hr rest. The right y-axis shows the extracted diffusion coefficient during lithation that calculate using eq (1) (see Weppner and Huggins, [3]):

$$(1) \quad D_{Li^+} = \frac{4}{\pi}\left(\frac{V_M}{SFz_i}\right)^2 \left[I_0\left(\frac{\delta E}{\delta x}\right)/\left(\frac{\delta E}{\delta\sqrt{t}}\right)\right]^2$$

Where $\frac{\delta E}{\delta x}$ is the slope of the open circuit voltage vs Li$^+$ concentration, z is the charge number (valence), F is the Faraday constant (96490 C mol^{-1}), V_M is the molar volume, S is the geometrical electrode area.

References

(1)   Patterson, A. R.; Elizalde-Segovia, R.; Wyckoff, K. E.; Zohar, A.; Ding, P. P.; Turner, W. M.; Poeppelmeier, K. R.; Narayan, S. R.; Clément, R. J.; Seshadri, R.; Griffith, K. J. Rapid and Reversible Lithium Insertion in the Wadsley–Roth-Derived Phase NaNb$_{13}$O$_{33}$. *Chem. Mater.* **2023**, *35*, 6364–6373. https://doi.org/10.1021/acs.chemmater.3c01066.

(2)   Preefer, M. B.; Saber, M.; Wei, Q.; Bashian, N. H.; Bocarsly, J. D.; Zhang, W.; Lee, G.; Milam-Guerrero, J.; Howard, E. S.; Vincent, R. C.; Melot, B. C.; Van der Ven, A.; Seshadri, R.; Dunn, B. S. Multielectron Redox and Insulator-to-Metal Transition upon Lithium Insertion in the Fast-Charging, Wadsley-Roth Phase PNb$_9$O$_{25}$. *Chem. Mater.* **2020**, *32*, 4553–4563. https://doi.org/10.1021/acs.chemmater.0c00560.

(3)   Weppner, W.; Huggins, R. A. Determination of the Kinetic Parameters of Mixed-Conducting Electrodes and Application to the System Li$_3$Sb. *J. Electrochem. Soc.* **1977**, *124*, 1569. https://doi.org/10.1149/1.2133112.